Limits of three-dimensional target detectability of logging while drilling deep-sensing electromagnetic measurements from numerical modelling

Nazanin Jahani[1,2] | **Carlos Torres-Verdín**[2] ⬤ | **Junsheng Hou**[2]

[1]Energy Department, NORCE Norwegian Research Centre, Bergen, Norway

[2]Hildebrand Department of Petroleum and Geosystems Engineering, University of Texas, Austin, Texas, USA

Correspondence
Nazanin Jahani, Energy Department, NORCE Norwegian Research Centre, Bergen, Norway. Email: naja@norceresearch.no

Abstract

Subsurface energy resources are often found in three-dimensional and non-spatially continuous rock formations that exhibit electrical anisotropy. Deep-sensing tri-axial borehole electromagnetic measurements are currently being used to detect three-dimensional fluid-bearing subsurface formations, but borehole environmental, geometrical and instrument-design factors, together with measurement noise, constrain their practical range of detection and spatial resolution. By understanding the interplay of the above factors on the detectability and sensitivity of borehole deep electromagnetic measurements, one can potentially quantify the uncertainty of both target spatial location (relative to the well trajectory) and electrical resistivity contrast, thereby improving the certainty of three-dimensional well navigation in real time. We implement a finite-volume method to numerically solve Maxwell's equations for three-dimensional electrically anisotropic heterogeneous rock formations in the calculation of magnetic fields measured with deep-sensing tri-axial borehole electromagnetic instruments. The calculated magnetic fields at measurement locations are described as the per cent difference between measurements acquired in rock formations with and without conductive or resistive three-dimensional targets. We quantify the maximum radial distance of detection from the well trajectory and the spatial sensitivity of a commercially available deep-sensing electromagnetic instrument with respect to environmental factors and measurement acquisition parameters by assuming that the borehole electromagnetic instrument can reliably detect offset three-dimensional targets if the corresponding per cent measurement difference exceeds the threshold for measurement noise. Results indicate that commercially available tri-axial deep-sensing borehole electromagnetic instruments can achieve maximum detection distances between a quarter of and a full transmitter–receiver spacing. In addition, we show that radial detection distances vary from 0.3 to 2 skin depths depending on the geological environment, that is, target conductivity contrast with respect to the embedding background, electrical anisotropy of the background formation and targets and measurement acquisition parameters, that is, frequency and transmitter–receiver spacings. The above findings are not only important

for instrument design and measurement-acquisition planning but also for the effective implementation of real-time inversion-based measurement interpretation procedures.

INTRODUCTION

In challenging subsurface geological environments, such as electrically conductive shale formations surrounding disconnected sandstone bodies (target), three-dimensional (3D) well geosteering is often used to adjust the well trajectory in real time based on the interpretation of electromagnetic (EM) fields excited and measured by antennas mounted on the drill string. The measured EM fields chiefly originate from electrical currents induced in rocks around the well trajectory.

Deep-sensing borehole tri-axial EM measurements were commercialized in the last 10 years to extend the ranges of radial and azimuthal sensitivity and resolution in the detection of electrically conductive rocks around the well trajectory (Clegg et al., 2019; Sinha et al., 2022; Thiel & Omeragic, 2020). They are interpreted as multi-dimensional spatial images of electrical resistivity via sophisticated and central processing unit intensive inversion techniques. Inversion-based interpretation results are often subject to great uncertainty due to non-uniqueness which can cause incorrect geological interpretations (i.e., incorrect target location, electrical resistivity, and shape) and sub-optimal geosteering decisions. One of the key sources of uncertainty in inversion-based interpretation results is the limited spatial resolution due to the inherent diffusive nature of borehole EM induction measurements (Antonsen et al., 2022).

The maximum distance of detection of borehole EM induction instruments is determined by the distance at which the measured magnetic field is approximately equal to the measurement noise within a specific borehole or geological environment. Additionally, the magnetic field excited in one-dimensional (1D) geological media is governed by EM measurement acquisition properties, perturbations of formation conductivity and the fraction of the probing distance with respect to skin depth (Ellis & Singer, 2007). The formula for skin depth can be found in Equation (A.10). For the case of a magnetic dipole source in the presence of 1D conducting media, it can be shown that (under ideal conditions) the maximum depth of detection of secondary magnetic fields can far exceed the skin depth. However, realistic geological environments are neither ideal nor one dimensional, whereby the range of detectability is typically much shorter than 1 skin depth. A number of geological environmental conditions limit the radial range of detectability of borehole

EM instruments, including the electrical properties of target and embedding background formations (e.g., electrical anisotropy and resistivity contrast) as well as measurement acquisition parameters. In order to obtain reliable geological interpretations of the measurements and make robust geosteering decisions, it is imperative to quantify both the spatial resolution of the borehole EM instrument and its range of detectability with respect to specific limiting parameters.

Several authors have attempted to ascertain the detectable range of EM instruments, but none have considered the radial range of detectability of a tri-axial borehole EM instrument across 3D geological environments exhibiting electrical anisotropy. Spies (1989) solved 1D fields and related the depth of investigation of the EM sounding tool to the geological and measurement acquisition parameters by calculating the highest frequency at which a homogeneous layer beneath a uniform layer would be detectable. Huang (2005) described the factors affecting the depth of detection for a small EM measuring instrument with short transmitter–receiver spacings. Rabinovich et al. (2012) defined the reliable depth of detection of an EM borehole instrument by mapping the sensitivity function (solving the sensitivity of the measured signal to local variations of electrical conductivity in the spatial region between transmitters and receivers) for different EM instrument configurations. Rabinovich et al. (2012)'s model included a very large background resistivity, whereby the skin effect was negligible. The same authors did not consider anisotropic background formations in their analysis. Puzyrev et al. (2018) studied the sensitivity of EM borehole instruments to resistive and conductive targets located away from the wellbore in heterogeneous formations via 3D numerical modelling and inversion. Their 3D models, however, did not consider the electrical anisotropy of both embedded targets and background formations.

Our study focuses on determining (a) the maximum radial distance of detection away from the well trajectory and (b) the spatial sensitivity to 3D subsurface targets for a commercially available tri-axial deep-sensing borehole EM instrument operating in spatially complex formations with respect to (a) measurement acquisition parameters, (b) distance between the well trajectory and the targets and (c) embedding geological environment.
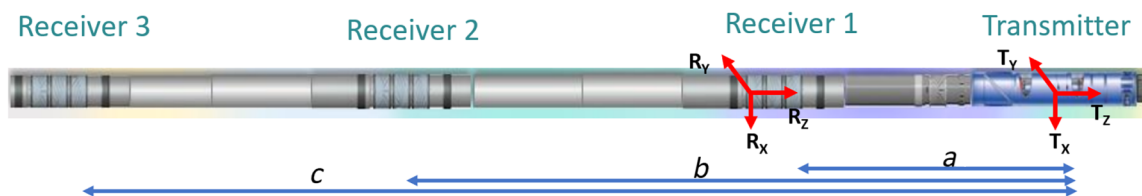
FIGURE 1 Schematic of the deep-sensing triaxial borehole EM logging instrument assumed in this paper, which is adapted from a commercial tool. The transmitter–receiver spacings are $a = 7.6$, $b = 15.24$ and $c = 30.5$ m. The transmitter and receivers have three tilted antenna coils.
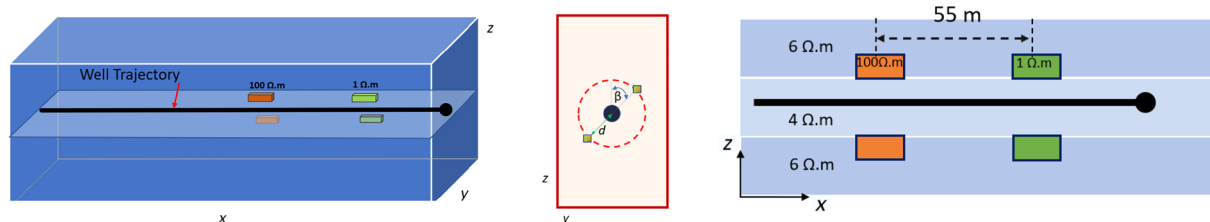

FIGURE 2 Case 3.1: Four electrically isotropic 3D targets of equal size, two resistive (100 ohm-m) and two conductive (1 ohm-m) are embedded in an isotropic nearly homogeneous formation with the resistivity of 4–6 ohm-m. The target radial distance (d) with respect to the well trajectory is fixed at 4.66 m in case 3.1, while the target's strike angle is $\beta = 11°$ and $79°$. Target's strike angle is $\beta = 45°$ for different experiments.

To that end, we construct several synthetic examples and solve the corresponding coupled 3D scalar–vector potential equations in the frequency domain to calculate magnetic fields across 3D heterogeneous and anisotropic formations, which include target bodies with high conductivity/resistivity contrasts. Simulation results allow us to generalize the spatial sensitivity range of borehole EM instruments as a function of skin depth and transmitter–receiver spacing.

Our study is based on a variety of fundamental 3D target conditions and the corresponding simulations of deep-sensing borehole measurements. Results from these numerical simulations and their consequences concerning distance of investigation and sensitivity should be regarded as a precursor of formal inversion studies, where non-uniqueness and regularization (spatial smoothing) of results become relevant.

The remainder of this paper is organized as follows: We introduce our method to solve EM equations across complex 3D formations in the second section. The third section describes the 3D synthetic examples constructed for our study and the corresponding numerical simulations of measurements acquired with a commercial borehole instrument. The description is centred on the per cent measurement differences due to the presence of 3D conductive and resistive targets offset from the well trajectory. We discuss the computational efficiency of our numerical methods in the fourth section. The last section summarizes the salient conclusions stemming from our work concerning the sensitivity and definition of 3D targets with deep-sensing borehole EM measurements.

METHOD

We solve Maxwell's equations numerically scalar–vector potential formulation for three-dimensional (3D) heterogeneous, electrically anisotropic media (Hou et al., 2006). The partial differential equations are given in Appendix A.1 (Equations A.1 and A.2); their solution is achieved with a finite-volume discretization method using Yee's staggered grid (Yee, 1966).

Grid design and node spacing affect the convergence, stability and accuracy of the numerical simulations. We employ a non-uniform Cartesian grid surrounding both the transmitter and receivers. We design the grid size locally by estimating an initial skin depth (hence electromagnetic [EM] instrument sensitivity) for a homogeneous medium at each measurement position. Where sensitivity is highest, grid cells are smallest, for example, in the neighbourhood of transmitters/receivers (a minimum spacing of 0.025 m) with the highest sensitivity, and they expand exponentially as the distance from the transmitter and receiver increases. This expansion follows a stepwise pattern as outlined by Davydycheva et al. (2003). The grid moves with the EM instrument along the well trajectory and across the formation model, and its stepwise increase continues until it reaches the outer boundary situated at a distance of 1–2 skin depths away from the lowest frequency of significance (Hou et al., 2006).

The linear system of equations from finite-volume discretization is asymmetric and complex-valued; we solve it iteratively using the complex biconjugate gradient algorithm. To accelerate its iterative rate of convergence, we
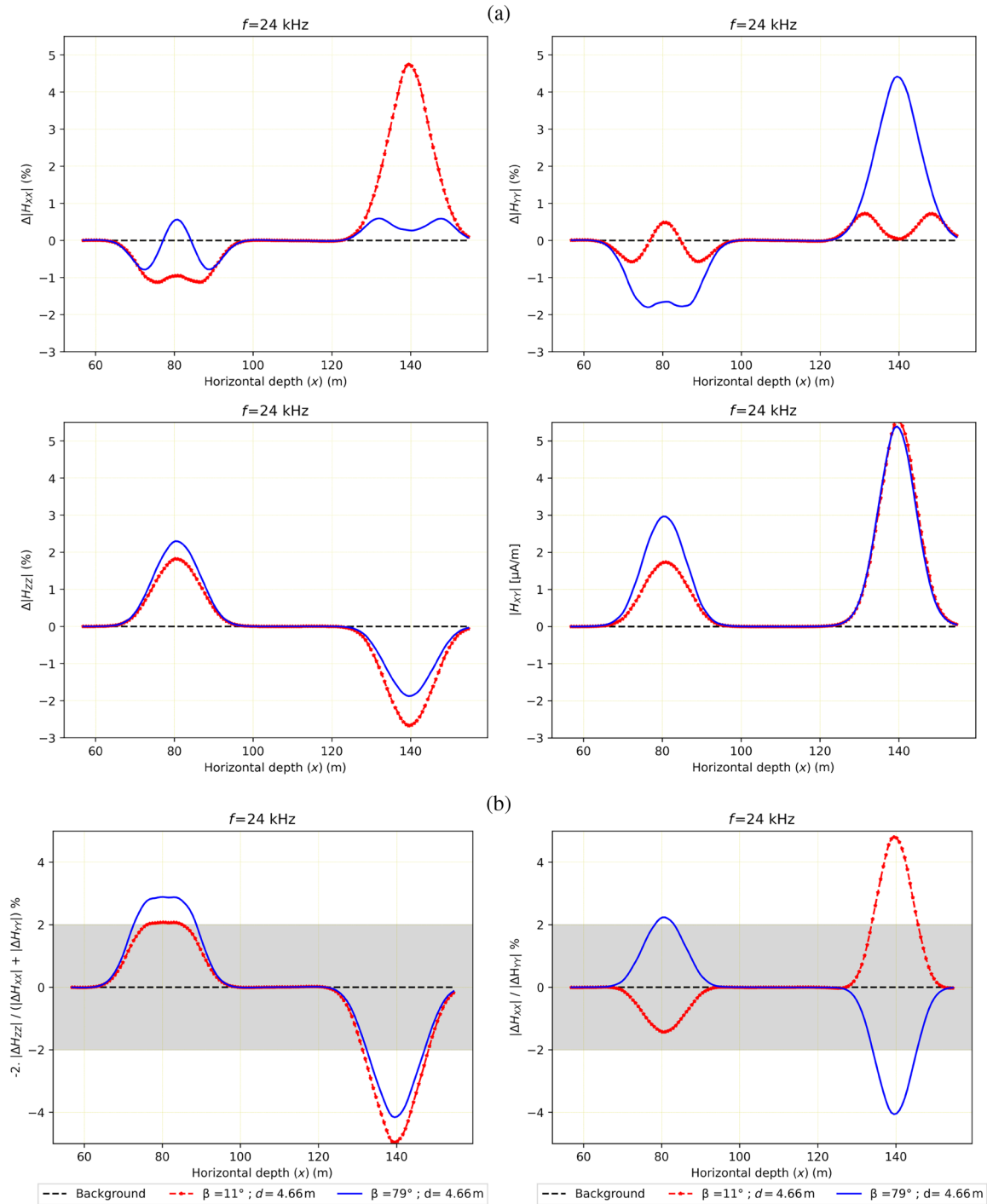
FIGURE 3 Case 3.1, effect of 3D target orientation on the measured magnetic field. (a) Coupled components (XX, YY, ZZ) of ΔH and H_{XY} and (b) harmonic resistivity and harmonic anisotropy. The grey zone indicates the measurement noise.

precondition the linear system before attempting its solution. As in Hou et al. (2006), we use the symmetric successive over-relaxation preconditioning strategy, which exhibits faster convergence rates than Jacobi preconditioning.

Because 3D computation is central processing unit (CPU) time intensive, we improve its speed by effective parallelization on CPU clusters available on the Stampede2 Linux cluster at UT Austin's Texas Advanced Computing Center (TACC).

To that end, we use TACC's SKX compute nodes with a CPU clock rate of 2.1 GHz. We ran a message passing interface across a cluster of processes; each process handles a number of logging points, computes their computational domain and stores their results (computed magnetic/electric field and voltage).

The deep-sensing triaxial borehole EM logging instrument assumed in this study is inspired by a commercially available
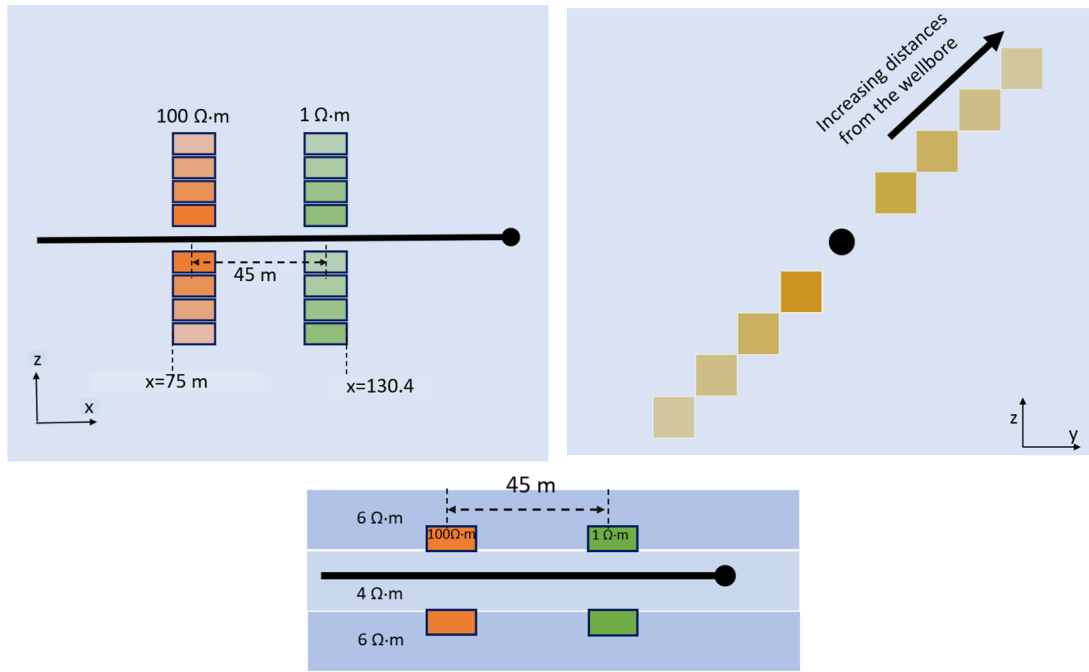
FIGURE 4 Case 3.1, two resistive (100 ohm-m) and two conductive (1 ohm-m) 3D targets are embedded in an isotropic nearly homogeneous formation and located around the well trajectory. For each case, there are four 3D targets of equal size, which are moving away from the well trajectory such that the target's radial distance from the well trajectory progressively increases.

tool which consists of one transmitter coil behind the drill bit and three arrays of receivers located behind the transmitter (Ezioba & Denichou, 2014). Figure 1 is a schematic of the EM instrument, which is mounted along a logging-while-drilling borehole assembly operating at five frequencies: 2, 6, 12, 24, and 48 kHz, where its configuration allows for variable transmitter–receiver spacings of 7.6, 15.24 and 30.5 m (25, 50 and 100 ft).

We calculated the amplitude of the magnetic field as the percentage difference between simulation results obtained for formations with and without high-contrast resistive and conductive 3D targets. Additionally, we assumed that the borehole EM instrument can reliably detect targets if the measurement percentage difference exceeds the threshold for measurement noise, which is assumed zero-mean 2% Gaussian. The transmitter and receivers have three tilted antenna coils in X, Y and Z directions, and the measured magnetic fields are represented by a tensor of nine components: with coupled (H_{XX}, H_{YY}, H_{ZZ}) and cross-coupled components (H_{XY}, H_{YX}, H_{XZ}, H_{ZX}, H_{YZ}, H_{ZY}), and its associated conductivity tensor is defined in Appendix A.2 (Equations A.3–A.9). Numerical results are described by plotting coupled components, shown as percentage differences and indicated with ΔH_{XX}, ΔH_{YY} and ΔH_{ZZ}. The percentage differences are defined as $\Delta H_K = \frac{H_t - H_b}{H_b} \times 100$, where K indicates XX, YY and ZZ, H_t is the magnetic field in formation with embedded tar-

gets, and H_b is the background field. Likewise, we plot the cross-coupled components XY or YX of the magnetic field, which is indicated by H_{XY}; note that in our cases in the third section all Z-related cross-coupled components (H_{XZ}, H_{ZX}, H_{YZ}, H_{ZY}) are null. The first subscript of all tensor components denotes the transmitter, and the second subscript denotes the receiver. In addition to a nine-component tensor of the magnetic field amplitude, we plot two other types of standard measurements: the harmonic anisotropy [$\Delta(H_{XX}/H_{YY})$] and the harmonic resistivity [$-2\,\Delta(H_{ZZ}/(H_{XX} + H_{YY}))$]. These measurements are industry standard for inversion-based interpretation, and each one of them is sensitive to different geometrical properties of the subsurface conductivity such as layer boundaries, anisotropy and resistivity (Davydycheva et al., 2020; Seydoux et al., 2014). The measurements are taken at the middle of the midpoint of the transmitter–receiver spacing, and after post-processing they are transferred to the position of the transmitter for plotting.

We verified the accuracy of numerical simulations obtained with our 3D finite-volume solver by comparing them to results obtained with a one-dimensional (1D) (i.e., case of transverse-isotropic horizontal layers) semi-analytical algorithm developed by Shahriari et al. (2018). Appendix B describes the comparison of 3D and 1D results. Figure B.2 illustrates that there was a difference of less than 1% between
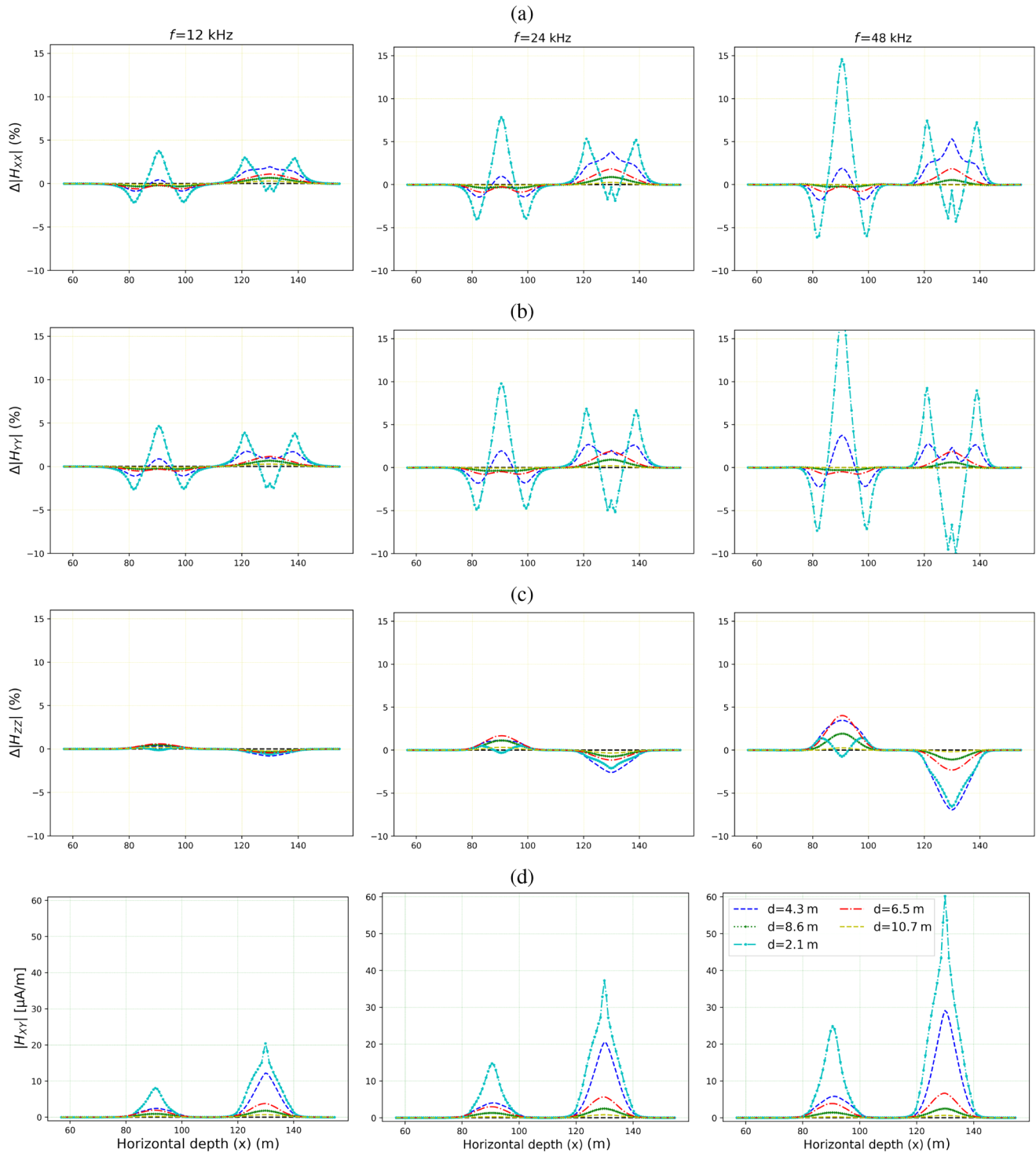
FIGURE 5 Case 3.2: EM measurement sensitivity for 3D targets embedded in our background formation: (a) ΔH_{XX}, (b) ΔH_{YY}, (c) ΔH_{ZZ} and (d) $|H_{XY}|$. Targets are located at varying radial distances d with respect to the well trajectory, with a fixed strike angle, $\beta = 45°$, while measurements are acquired at different frequencies.

the two results for calculated magnetic fields across a variety of three-layer horizontally homogeneous formations.

In the following sections, we describe the numerically simulated measurements obtained for several relevant synthetic examples.

SYNTHETIC EXAMPLES AND NUMERICAL RESULTS

We quantify the maximum radial distance of detection away from the well trajectory and the spatial sensitivity of a
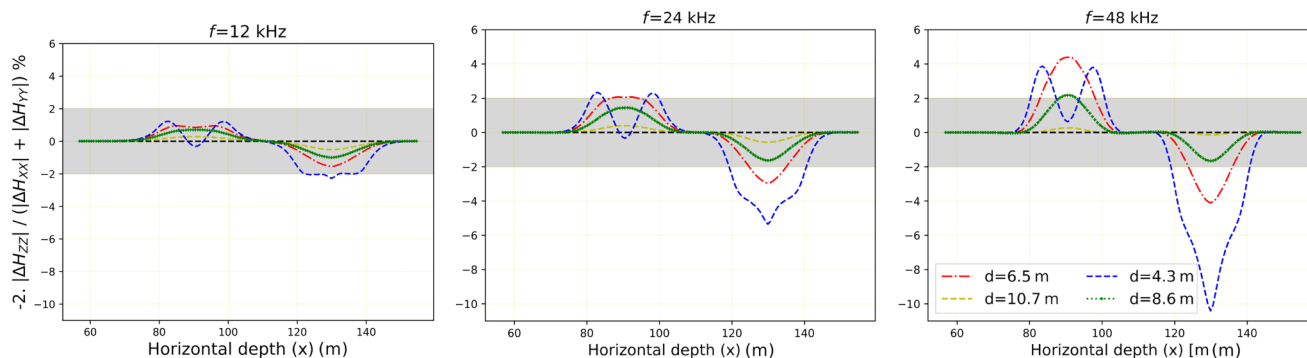
FIGURE 6 Case 3.2: Harmonic resistivity measurement acquired at 12, 24, and 48 kHz for the same example shown in Figure 4. For all cases $\beta = 45°$. The grey zone indicates measurement noise.
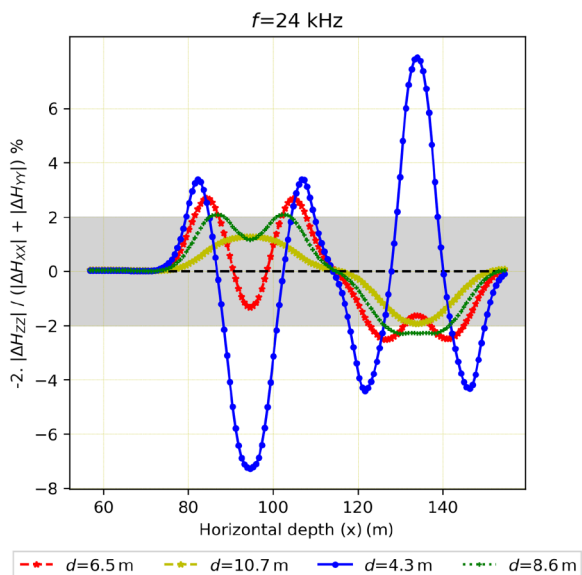

FIGURE 7 Harmonic resistivity measurement at 24 kHz with a transmitter–receiver spacing of 15.24 m. The grey zone indicates the measurement noise.

FIGURE 8 Case 3.3: Two resistive (100 ohm-m) and two conductive (1 ohm-m) 3D targets embedded in isotropic nearly homogeneous background formations with (a) low and (b) high resistivities.

commercially available deep-sensing electromagnetic (EM) instrument with respect to

- the orientation and distance of the three-dimensional (3D) target bodies relative to the well trajectory,
- the measurement acquisition parameters (i.e., frequency and transmitter–receiver spacing),
- the electrical conductivity and anisotropy of the background formation and
- the electrical conductivity and anisotropy of 3D target bodies embedded within the background formation.

Five synthetic cases are considered in the study. Figures 2, 4, 8, 10, and 12 show target geometries and locations, well trajectory positions relative to targets and background formation details for each synthetic example. In all examples,
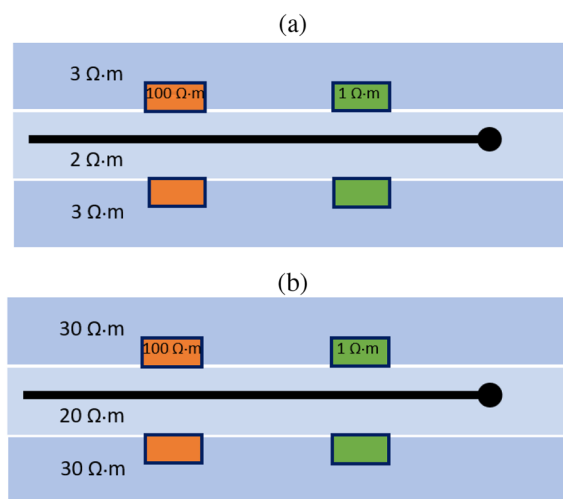
the background formation has several layers with a thickness of 3.05 m. The layers have small-scale variations of resistivity. The background formation is azimuthally symmetric around the axis of the well trajectory and embedded four target cuboid bodies: two targets are resistive, and two are conductive. The well trajectory is located at the vertical centre of the middle layer of the background formation and is horizontal along the x-axis of the formation coordinate and the four targets with high resistivity contrast with respect to the embedding formation are located around the well trajectory in the yz plane. In our approach, the rationale behind selecting a horizontal well trajectory is rooted in practical considerations. The navigation of high-angle and horizontal wells is a recurring theme in spatially complex rocks and is crucial when the aim is to enhance spatial contact with hydrocarbon-bearing formations to improve production. Furthermore, the selection of high-angle and horizontal wells gains greater
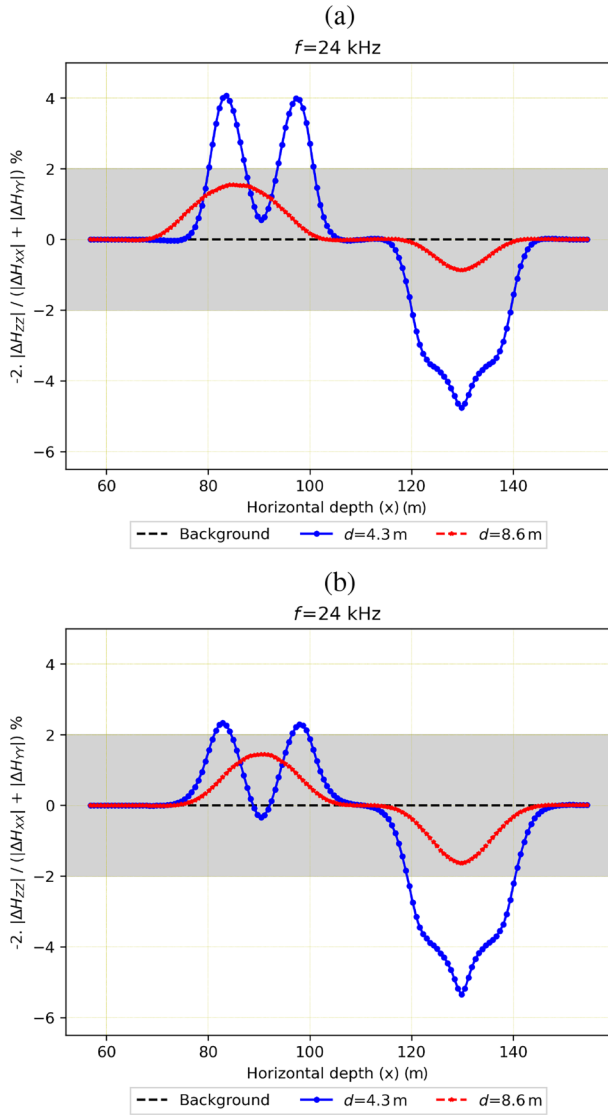
(a)

(b)

FIGURE 9 Case 3.3: Measurement sensitivity as a function of background formation resistivity. The plots compare the EM measurement sensitivity, indicated with percentage differences of harmonic resistivity measurements of the model in Figure 8: (a) low resistivity (2–3 ohm-m) and (b) high resistivity (20–30 ohm-m) background formations. The grey zone indicates the measurement noise. For all cases $\beta = 45°$.
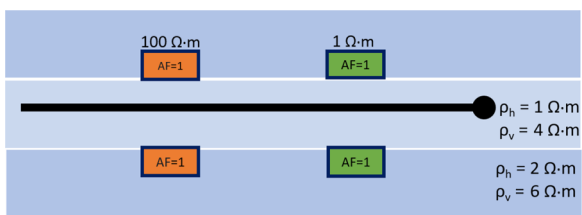

FIGURE 10 Case 3.4: Isotropic 3D targets embedded in electrically anisotropic formations with an anisotropy factor of AF = 3 for the top and bottom layers and AF = 4 for the middle layer. The thickness of the layers is 3.05 m.

significance in situations where anisotropy and the presence of an embedding one-dimensional medium substantially influence the detection capabilities of deep borehole EM measurements.

In all examples, four targets are embedded: two resistive and two conductive. Each target is 9.15 m (30 ft) along x, 3.05 m (10 ft) along y and 3.05 m (10 ft) along z in the formation coordinate system. Dimension and size for the latter targets were selected based on numerical accuracy. These small targets can represent sandstone injectites overlying shale (Bradaric et al., 2022). Even though the shape of the target does affect measurement sensitivity, especially when located near EM transmitters and/or receivers, our studies indicate that the selected shapes are adequate to quantify measurement sensitivity and target detectability in the mid- to far-regions of detection away from the well trajectory.

The computational domain is divided into $N_X \times N_Y \times N_Z$ rectangular cells in the X, Y and Z directions in the well trajectory coordinate system. There are approximately 800,000 to 1 million grid cells included in the numerical simulations. The smallest grid-cell volume is about 15 cm^3 around the transmitters/receivers, and their volume will increase exponentially as they move away from transmitters/receivers. The well trajectory is divided into 144 logging positions, spaced at 0.46 m (1.5 ft), intervals and are distributed over 48 cores of UT Austin's Texas Advanced Computing Center's SKX compute nodes.

Each synthetic example includes several variables for consideration:

- Case 3.1: strike angle relative to the well trajectory ($\beta = \arctan(y/z)$) of the 3D target;
- Case 3.2: radial distance of the 3D target from the well trajectory (d), operating frequency of EM instrument (f) and transmitter–receiver spacing (λ);
- Case 3.3: radial distance of the 3D target from the well trajectory (d) and background formation resistivity ($\rho = 1/\sigma$);
- Case 3.4: radial distance of the 3D target from the well trajectory (d) and background formation anisotropy factor (AF; σ_h/σ_v);
- Case 3.5: embedded target AF (σ_h/σ_v).

The strike angle of the 3D target with respect to the horizontal well trajectory is variable only in case 3.1, while it is fixed at 45° in all other examples. For all examples except for case 3.2, the tool operating frequency is 24 kHz and transmitter–receiver spacing is 7.62 m (25 ft). Likewise, for all examples, measurement noise is assumed zero-mean 2% Gaussian.
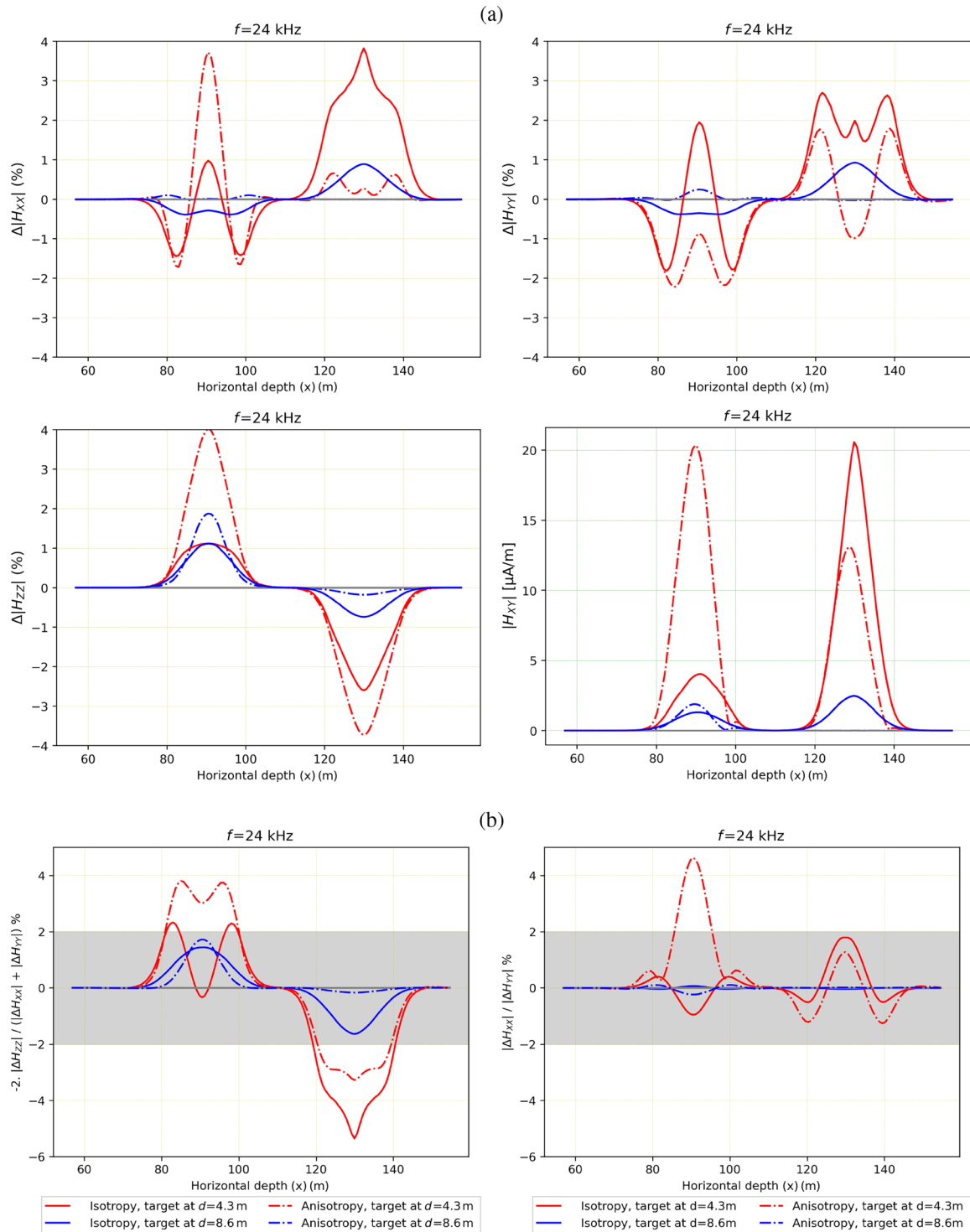
(a)

(b)

FIGURE 11 Case 3.4: Effect of formation anisotropy on measurement sensitivity. Solid curves identify electrically isotropic background formations, while dashed curves identify anisotropic background formations shown in Figure 10, and $\beta = 45°$ for all cases. (a) coupled (XX, YY, ZZ) components of ΔH and H_{XY}, (b) harmonic resistivity and harmonic anisotropy. The grey zone indicates the measurement noise.

Target with variable strike angle with respect to the well trajectory

Here, we quantify the impact of target orientation on borehole EM measurement sensitivity. Figure 2 shows the conductive

and resistive 3D targets around the well trajectory, with a radial distance of d. The targets are embedded in an isotropic nearly homogeneous background formation with the resistivity of 4–6 ohm-m. Conductive and resistive targets are grouped at two different points on the x-axis. The resistive
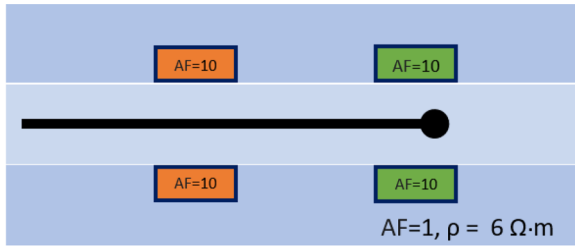
FIGURE 12 Case 3.5: Electrically anisotropic 3D targets embedded in an isotropic formation with a resistivity of 6 ohm-m (bottom and top layers) and 4 ohm-m (middle layer). Horizontal and vertical resistivities for resistive targets (ρ_h and ρ_v) are (i) 50 and 100 ohm-m and (ii) 10 and 100 ohm-m, while for conductive targets ρ_h and ρ_v are (i) 0.5 and 1 ohm-m and (ii) 0.1 and 1 ohm-m, whereby the corresponding target AF are (i) 2 and (ii) 10. The target radial distance from the well trajectory is 4.3 m.

targets are between $x = 66.75$ m and $x = 75.9$ m, and conductive targets are between $x = 121.6$ m and $x = 130.75$ m. The 3D targets are placed at two different strike angles with respect to the horizontal well trajectory: $\beta = 79°$ (corresponding to $y = \pm4.57$ m and $z = \pm0.91$ m and $\beta = 11°$ (corresponding to $y = \pm0.91$ m and $z = \pm4.57$ m). The radial distance from the well trajectory in this example is $d = 4.66$ m, which is approximately equivalent to 0.65 skin depths in the background medium.

Figure 3a shows that ΔH_{XX} and ΔH_{YY} exhibit significantly different behaviour with respect to the two values of β, whereas ΔH_{ZZ} and H_{XY} do not. Furthermore, all components of the EM measurements detect the conductive target with good sensitivity except for ΔH_{YY} at $\beta = 11°$ and ΔH_{XX} at $\beta = 79°$. Additionally, Figure 3b shows that β does not affect the sensitivity of either harmonic anisotropy or harmonic resistivity measurements. A final observation is that EM measurements have twice the sensitivity to conductive targets than to resistive ones. Due to slightly inhomogeneous background formation, the curve of ΔH_{XX} at $\beta = 11°$ differs slightly from the curve of ΔH_{yy} at $\beta = 79°$ as well as the two curves of ΔH_{ZZ}.

Variable radial distance with respect to the well trajectory

In this example, four configurations are shown; each of which has four embedded targets that get further away from the well trajectory. Comparing this example to case 3.1, β is 45°, d has four variations and the distance between resistive and conductive targets is 45 m.

Here, we estimate the radial distance from the well trajectory up to which the borehole EM instrument can detect 3D targets with measurable sensitivity. The targets in this example are diagonally located on the yz plane at steps of 1.52 m (5 ft) in both the y and z axes. The resistive target horizontal locations are from $x = 75$ m to $x = 84.14$ m, and the conductive targets are from $x = 121.3$ m to $x = 130.45$ m (see Figure 4). The four targets are embedded in an isotropic nearly homogeneous background formation with a resistivity of 4–6 ohm-m. We compare the coupled components of ΔH, H_{XY} and the two measurement combinations (harmonic anisotropy and harmonic resistivity) with respect to distances from the well trajectory at different tool operating frequencies and transmitter–receiver spacings.

Effect of instrument operating frequency

Figures 5 and 6 describe how tool operating frequency affects EM instrument sensitivity. If the embedded conductive targets are at greater distances than $d = 4.3$ m and the resistive ones at greater distances than $d = 2.1$ m, the sensitivity of measurements at 12 kHz is below the assumed measurement noise (2%). At distances beyond these radial distances, the targets cannot be reliably detected. Moreover, the EM borehole instrument can detect both conductive and resistive targets at a frequency of 24 kHz at a radial distance of less than 6.5 m from the well trajectory. At 48 kHz, the EM borehole instrument can detect conductive targets at radial distances of less than $d = 6.5$ m, while resistive targets at less than $d = 8.6$ m. Therefore, measurements acquired with low-frequency instruments are more sensitive to conductive targets, while high-frequency measurements exhibit better sensitivity for resistive targets; however, Figures 5 and 6 also indicate that high-frequency measurements are subject to increasing dampening or a higher attenuation rate.

Effect of transmitter–receiver spacing

In this example, we increase the spacing between the transmitter and receiver to 15.24 m (approximately 2 skin depths) at a frequency of 24 kHz. Figure 7 indicates that the EM instrument can detect both conductive and resistive targets at a radial distance of less than 7.62 m from the well trajectory, equivalent to 1 skin depth or half of the transmitter–receiver spacing. In addition, as the distance between the transmitter and receiver increases from 7.62 to 15.24 m, measurement sensitivity becomes approximately four times greater in the case of targets located at the radial distance of 4.3 m (blue line). Figure 7 also shows that the sensitivity of measurements acquired at the radial distance of more than 8.6 m exceeds the threshold for measurement noise (2%).

Variable resistivity of the embedding formation

Here we examine the effect of background formation resistivity on the detectability range and sensitivity of the deep-sensing borehole EM instrument. We construct two cases (Figure 8) with (a) low resistivity (2–3 ohm-m) and (b)
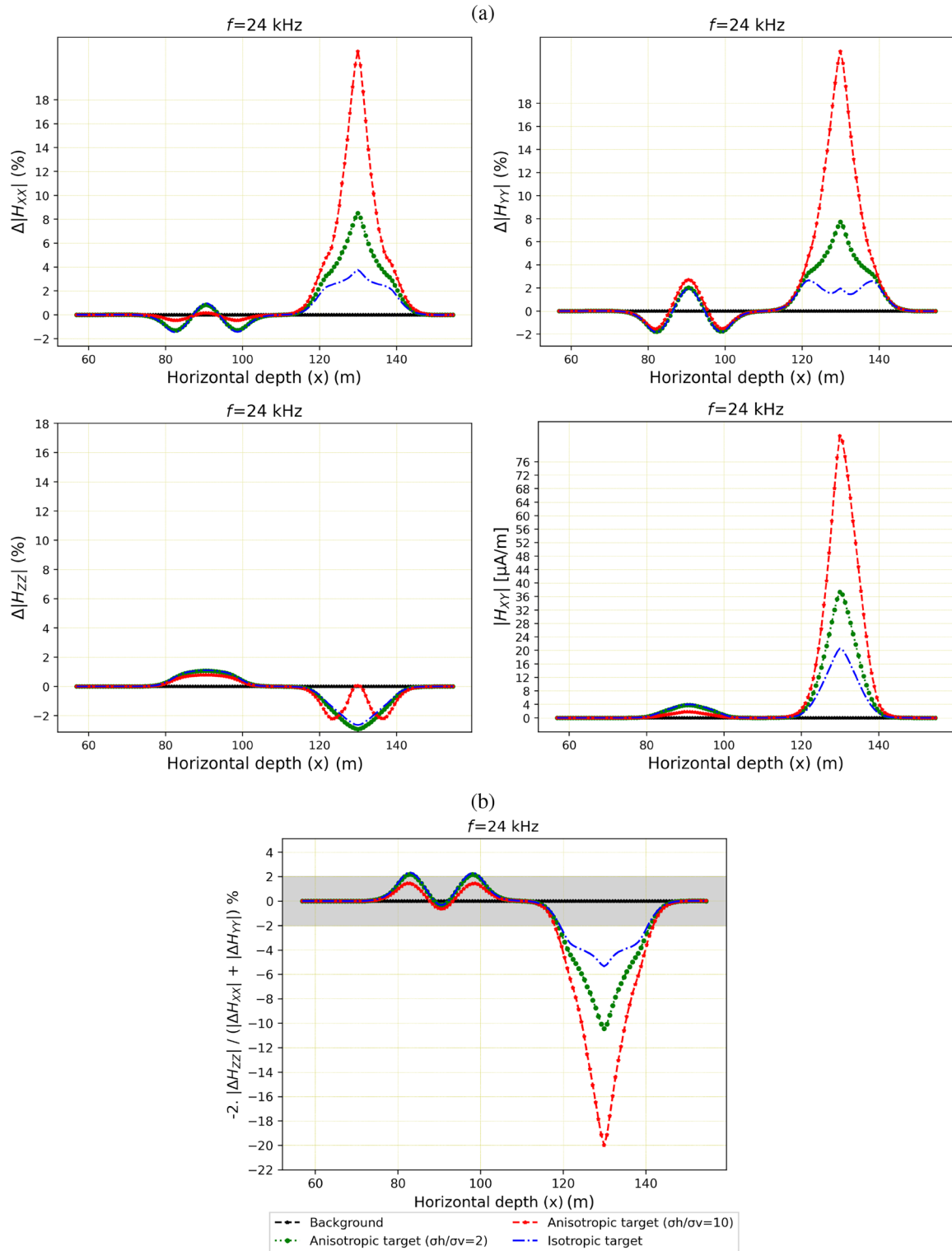
(a)

(b)

FIGURE 13 Case 3.5: Measurement sensitivity as a function of the electrical anisotropy of the embedded 3D target. The plots compare the measurement sensitivity of anisotropy effects with respect to isotropic targets embedded in an isotropic formation. Target distances from the well trajectory are 3.05 m in the y direction and 3.05 m in the z direction; equivalent to $d = 4.3$ m and $\beta = 45°$. (a) Coupled and cross-coupled components. (b) Harmonic resistivity. The grey zone indicates the measurement noise.
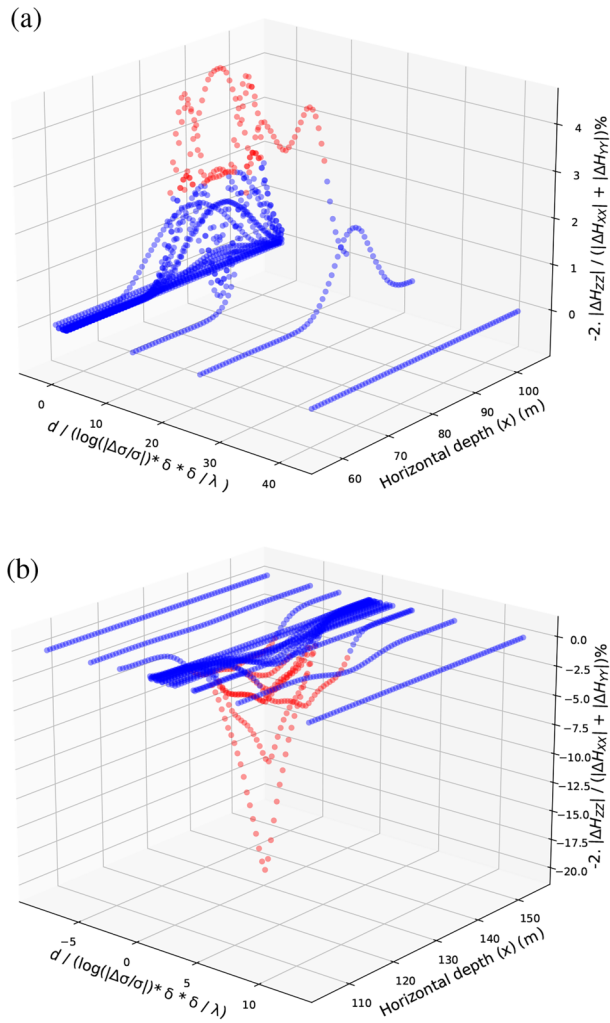
(a)

(b)

FIGURE 14 Comparison of EM measurement sensitivity in formations with embedded (a) resistive targets and (b) conductive targets. Measurement sensitivity in the vertical axis corresponds to percentage differences of harmonic resistivity measurements, for all the models described in Section 3. The x-axis describes the horizontal distance between the measurement position along the well trajectory and the targets, while the y-axis is the radial distance normalized to skin depth, transmitter–receiver spacing and conductivity contrast between background formation and embedded targets.

(a)

(b)

FIGURE 15 Measurement sensitivity described in the form of a scatter plot versus (a) target radial distance to skin depth and (b) target horizontal distance as well as radial distance to skin depth.

high resistivity (20–30 ohm-m) of the background formation; the associated measurements are shown in Figure 9. The thickness of the layers is 3.05 m. The well trajectory is located in the vertical centre of that middle layer. At $d <$ 4.3 m, the measurement sensitivity is twice as high for the case of resistive targets (100 ohm-m) in conductive environments (i.e., 2–3 ohm-m) compared to resistive environments (i.e., 20–30 ohm-m). Similarly, the conductive target (1 ohm-m) in case b is detected with better sensitivity due to the larger resistivity contrast. Additionally, the decay of the electromagnetic field over distance is less pronounced within the higher resistivity background, which likely plays a role in enhancing sensitivity within this resistive context.
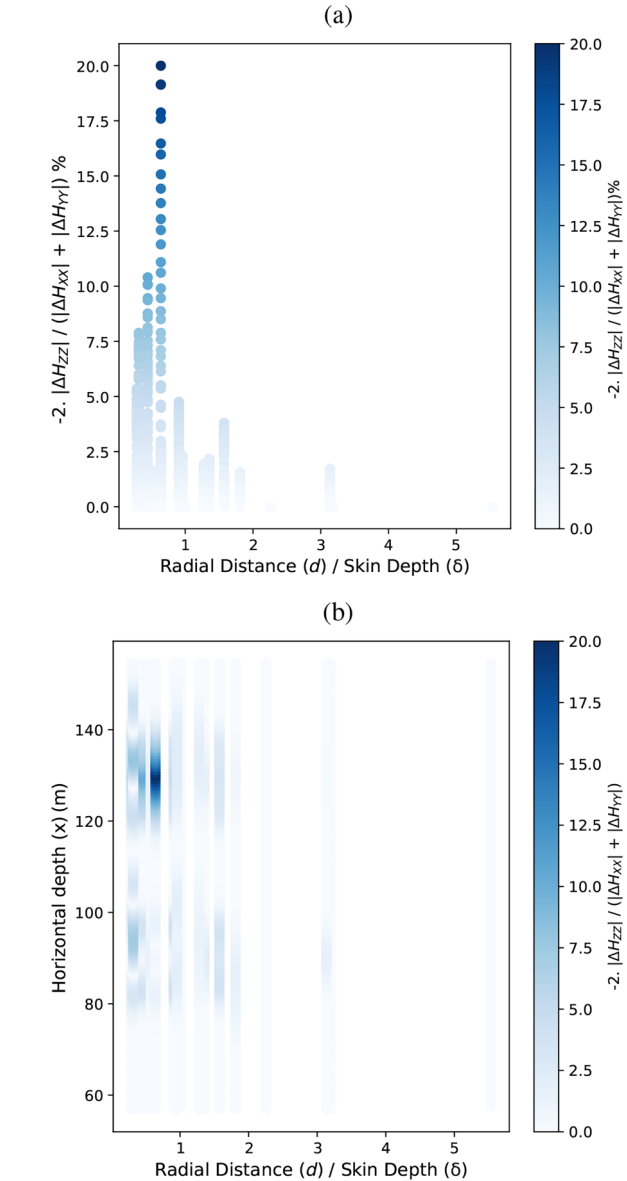
Background formations exhibiting electrical anisotropy

Thinly laminated sandstones or shale sequences behave macroscopically as electrically anisotropic formations, withdifferent parallel- and perpendicular-to-bedding plane resistivities. Electrical anisotropy affects the equivalent conductivity tensor of the medium (see Appendix A.2), especially in inclined or horizontal boreholes or bedding in the strike direction, impacting skin depth (Jahani & Jacob, 2015), attenuation rate, hence, the maximum detection distance of the EM measuring instrument (Anderson et al., 2001; Carcione, 2011).
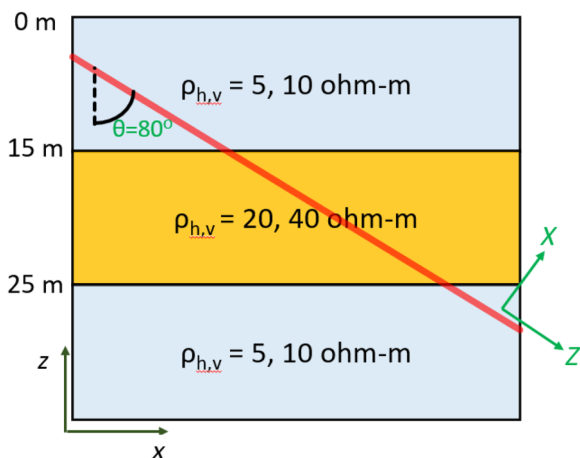
FIGURE B.1 Synthetic formation model composed of three homogeneous layers of varying resistivity together with an inclined well trajectory. The thickness of the middle layer is 10 m. The formation coordinate system is xyz, and the well trajectory coordinate system is XYZ.

In Figure 10, high-resistivity contrast targets, with respect to the background, are embedded in an electrically anisotropic background formation with an anisotropy factor of 3 and 4. Figure 11 compares the sensitivity of borehole EM measurements acquired in electrically isotropic background formations (red), with background resistivity of 4–6 ohm-m, to those of anisotropic formations (blue) for two different target locations with respect to the well trajectory: $d = 4.3$ m and $d = 8.6$ m. Electrical anisotropy of the background formation strongly influences measurement sensitivity and attenuation rate; the anisotropic factor affects the conductivity tensor, thereby changing the contrast between the target and the background thus the sensitivity of the measurements. Measurement sensitivity increases for resistive targets as the degree of anisotropy of the embedding formation increases, whereas it decreases for conductive targets as the degree of anisotropy increases. Furthermore, Figure 11 shows that measurement sensitivity to conductive targets embedded in anisotropic formations decreases rapidly. Therefore, the maximum radial length of detection for conductive targets decreases compared to that for resistive targets when increasing the electrical anisotropy factor; this behaviour is in agreement with the sensitivity analysis reported by Alumbaugh and Lu (2001).

Electrically anisotropic targets

In Figure 12, several electrically anisotropic targets are embedded in an isotropic homogeneous background formation. Because conductivity tensors are a combination of horizontal and vertical conductivity (Appendix A.2), the target's electrical anisotropy will affect its equivalent conductivity, its contrast with the formation, the induced current and the magnetic field attenuation. An example of the influence of target anisotropy on measurement sensitivity is shown in Figure 13: as the anisotropy factor increases from 2 to 10, the XX and YY components of ΔH and H_{XY} increase by about four times for conductive targets at the radial distance of 4.3 m with respect to the well trajectory. Nevertheless, at this radial distance, ΔH_{ZZ} decreases due to the large ZZ element in the conductivity tensor. The same figures also indicate that target anisotropy factors have a minor impact on the sensitivity to the resistive targets.

General observations

Figure 14 describes the EM measurement sensitivity for all synthetic examples considered in this paper with (a) embedded resistive targets and (b) embedded conductive targets. Measurement sensitivity is plotted as percentage differences of harmonic resistivity measurements (vertical axis (z)) versus radial distance from the wellbore to skin depth and transmitter–receiver spacing $\frac{d}{\delta} \frac{\lambda}{\delta}$ as well as to conductivity contrast between background formation and embedded targets $\Delta \sigma$ (y-axis) and horizontal distance between the target and the well trajectory (x-axis)). Red dots in Figure 14a,b indicate that measurement sensitivity is above measurement noise (2%), while blue dots designate conditions when measurement sensitivity is below measurement noise. EM measurements for the case of resistive targets have a maximum sensitivity of 4%, whereas the corresponding measurements for conductive targets have a sensitivity of 2–20%. Therefore, EM measurements acquired in the presence of conductive targets have higher sensitivity, but shorter distance of detection than for the case of resistive targets. Additionally, EM measurements are plotted as scatter colour dots versus radial and horizontal distances in Figure 15a,b. The latter figures indicate that measurement sensitivity is below measurement noise (2%) when the radial distance to skin depth exceeds 2.

COMPUTATIONAL EFFICIENCY

By making use of parallel central processing unit (CPU) calculations, we showed that for 144 logging positions distributed over 48 cores on a UT Austin's Texas Advanced Computing Center SKX compute node, with a CPU clock rate of 2.1 GHz, the run time for each logging point and each frequency is slightly less than 20 minutes and around 2000 MB of memory usage. When the number of logging points exceeds the number of CPU cores, total run-time increases linearly as the number of grid cells, transmitters–receivers and frequencies increase. Numerical simulations reported in this paper computed one logging point in series, with no immediate opportunity for CPU parallelization; however, matrix decomposition and the use of graphics processing unit threads for
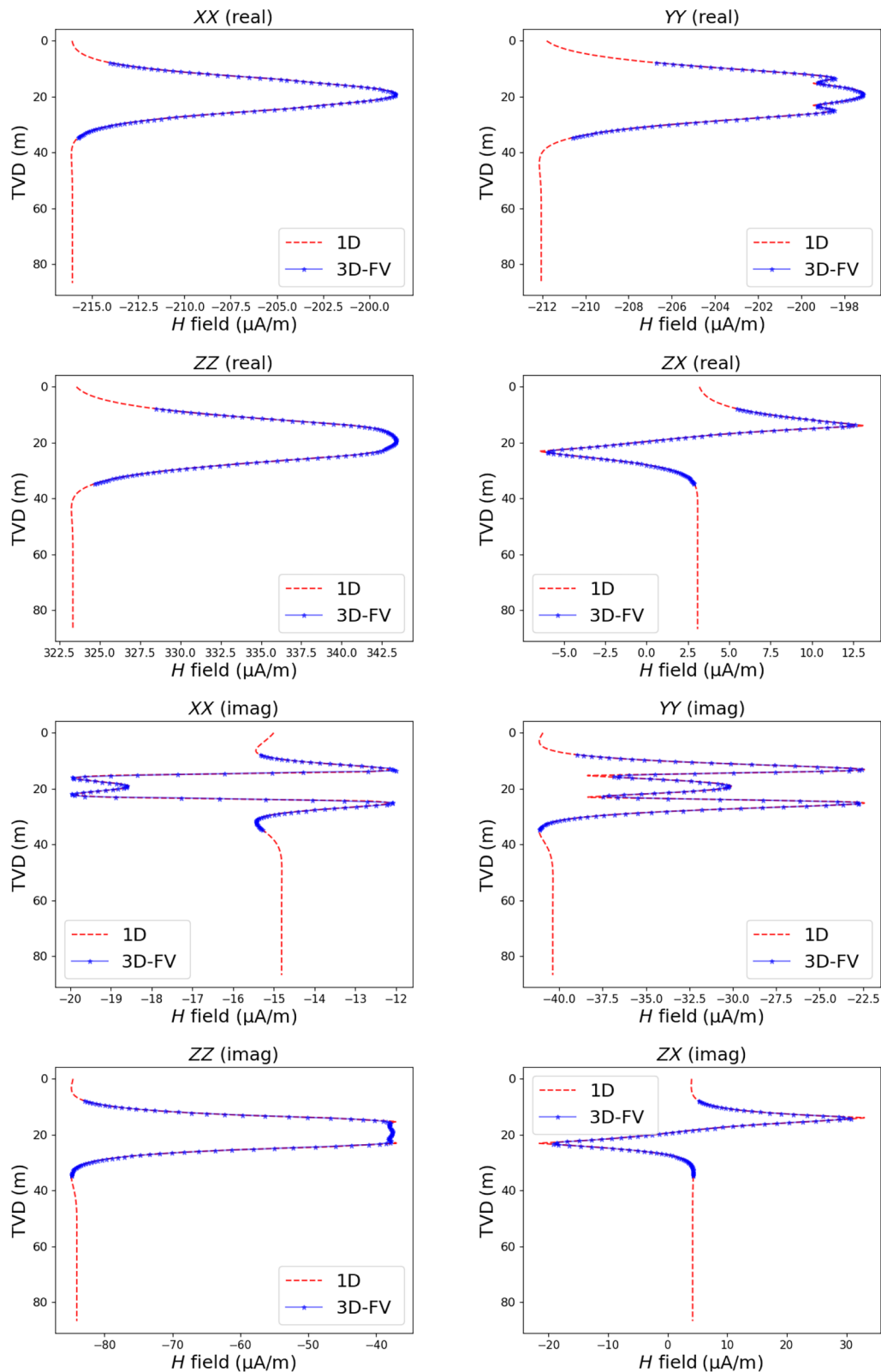
FIGURE B.2 Coupled and cross-coupled components of magnetic fields numerically simulated with 3D finite-volume and 1D semi-analytical algorithms for the synthetic model shown in Figure B.1. The EM instrument is configured at transmitter–receiver spacing of 7.62 m (25 ft) and the operating frequency is 12 kHz.

each element of the matrix could be used to further accelerate the computations.

CONCLUSIONS

Making use of the finite-volume method and parallel central processing unit computing, we numerically solved three-dimensional (3D) coupled scalar-potential equations in 3D geological environments, including spatially heterogeneous and electrically anisotropic 3D targets and embedding formations. We assumed zero-mean, 2% Gaussian measurement noise to quantify the spatial limits of sensitivity and detectability of a commercially available deep-sensing electromagnetic (EM) measuring instrument equipped with tri-axial transmitters and receivers with respect to (a) target orientation and distance from the well trajectory, (b) frequency of measurement acquisition and (c) conductivity and electrical anisotropy of both formation and 3D targets.

We observed that EM measurement resolution and target detectability are not affected by the orientation of 3D targets relative to the well trajectory when the radial distance between targets and well trajectory remains unchanged, but it will affect measurement polarity (sign), which can be used to determine target strike angle. On the other hand, the target's radial distance from the well trajectory and its electrical resistivity contrast with respect to its embedding formation, electrical anisotropy and measurement acquisition parameters influence both EM detectability range and measurement sensitivity.

Our study underscores the method's limitations, which were accentuated by our deliberate selection of smaller target bodies with inherently lower measurement resolutions when contrasted with larger targets. In our examples, the range of detectability of EM measuring instruments is shorter than 2 skin depths or shorter than the distance between transmitters and receivers. With a transmitter–receiver spacing of 7.62 m and a frequency of 12 kHz, borehole EM instruments can acquire measurements with a sensitivity of 2% when embedded conductive targets are located at radial distances of 4.3 m (0.6 δ) from the well trajectory. This frequency and radial distance, however, give rise to sensitivity below the measurement noise for resistive targets.

At a frequency of 24 kHz and a radial distance of 4.3 m (0.6 δ), measurement sensitivity to conductive targets is 4% and 2% to resistive targets. Moreover, at 24 kHz, the radial length of detectability increases to 6.4 m (0.9 δ)) with a measurement sensitivity of 2.5% for conductive targets and 2% for resistive targets. Likewise, at a frequency of 48 kHz and a radial distance of 8.5 m (1.7 δ)), measurement sensitivity is approximately 2% for resistive targets and below 2% for conductive targets. Our work indicates that the lower frequency EM measuring instrument (12 and 24 kHz) is

capable of detecting and defining conductive targets at relatively long radial distances from the well trajectory, whereas the higher frequency instrument (48 kHz) can detect and define resistive targets at relatively long radial distances. Due to their relatively short skin depth, the detectability range of both conductive and resistive targets decreases with increasing frequency.

Our synthetic examples indicate that detecting the spatial location of 3D geological targets at a given radial distance is possible when the conductivity contrast between the target and embedding background formation increases. Moreover, the conductivity tensor is influenced by the electrical anisotropy present in both the 3D target and the background formation. This, in turn, impacts the conductivity contrast between the target and the surrounding embedded background formation. Consequently, the magnetic field, detectability range and sensitivity of the EM measuring instrument are all affected. In our synthetic examples, measurement sensitivity increases for resistive targets from 2% to 4% as the degree of anisotropy of the embedding formation increases from one to four, while it decreases for conductive targets from 5% to 3% as the degree of anisotropy increases. Therefore, the maximum radial length of detection for conductive targets decreases compared to that for resistive targets when increasing the electrical anisotropy factor. Our synthetic examples indicate that increasing the anisotropic factor of background formations from 1 to 4 affects only measurement sensitivity but not the radial length of detectability. Additionally, we found that measurement sensitivity increases up to four times (from 5% to 20%) when the electrical anisotropy ratio of a conductive target increases by five times while the embedding formation remains isotropic.

Using the above factors as the basis for quantifying the ranges of detectability and definition of 3D offset targets by EM measuring instruments enables the assessment of the uncertainty of both target spatial location (relative to the well trajectory) and electrical resistivity contrast, thereby enhancing the accuracy of both geological interpretation and real-time 3D well geosteering. In addition, estimating the radial detectability range of borehole EM measurements has an immediate application in the design of adaptive numerical grids for 3D inversion procedures, as determining the optimal size and number of grid cells can translate into great savings in computational time: parallel computations and optimal grid design enable 3D stochastic inversion for real-time reservoir mapping and geosteering.

DATA AVAILABILITY STATEMENT

The data that support the findings of this study are available on request from the corresponding author. The data are not publicly available due to privacy or ethical restrictions.

ORCID

Carlos Torres-Verdín https://orcid.org/0000-0001-6628-4833

REFERENCES

Alumbaugh, D.L. & Lu, X. (2001) Three-dimensional sensitivity analysis of induction logging in anisotropic media. *Petrophysics*, 42(06).

Anderson, B., Barber, T. & Gianzero, S. (2001) The effect of cross-bedding anisotropy on induction tool response. *Petrophysics*, 42(02), 137–149.

Antonsen, F., Danielsen, B.E., Jensen, K.R., Prymak-Moyle, M., Lotsberg, J.K., Teixeira De Oliveira, M.E. et al. (2022) What next after a decade with significant advances in the application of ultra-deep azimuthal resistivity measurements? *Petrophysics*, 63(06), 762–780.

Bradaric, A.D., Andersen, T., Lecomte, I., Løseth, H. & Eide, C.H. (2022) Recognition and characterization of small-scale sand injectites in seismic data: implications for reservoir development. *Journal of the Geological Society*, 179(2), jgs2021-041.

Carcione, J.M. (2011) Electromagnetic diffusion in anisotropic media. *Radio Science*, 46(01), 1–11.

Clegg, N., Parker, T., Djefel, B., Monteilhet, L. & Marchant, D. (2019) The final piece of the puzzle: 3-D inversion of ultra-deep azimuthal resistivity LWD data. SPWLA-2019-HHH. In: *SPWLA 60th annual logging symposium*, The Woodlands, TX, June 2019. OnePetro.

Davydycheva, S., Druskin, V. & Habashy, T. (2003) An efficient finite-difference scheme for electromagnetic logging in 3D anisotropic inhomogeneous media. *Geophysics*, 68(5), 1525–1536.

Davydycheva, S., Druskin, V., Knizhnerman, L. & Rabinovich, M. (2020) Quality control of ultra-deep resistivity imaging using fast 3D electromagnetic modeling. In: *SEG technical program expanded abstracts 2020*. Houston, TX: Society of Exploration Geophysicists, pp. 380–384.

Ellis, D.V. & Singer, J.M. (2007) *Well logging for earth scientists*. Vol. 692, Dordrecht, The Netherlands: Springer.

Ezioba, U. & Denichou, J.M. (2014) Mapping-while-drilling system improves well placement and field development. *Journal of Petroleum Technology*, 66(08), 32–35.

Hou, J., Mallan, R.K. & Torres-Verdín, C. (2006) Finite-difference simulation of borehole EM measurements in 3D anisotropic media using coupled scalar-vector potentials. *Geophysics*, 71(5), G225–G233.

Huang, H. (2005) Depth of investigation for small broadband electromagnetic sensors. *Geophysics*, 70(6), G135–G142.

Jahani, S. & Jacob, Z. (2015) Photonic skin-depth engineering. *Journal of the Optical Society of America B*, 32(7), 1346–1353.

LaBrecque, D.J. (1999) Finite-difference modeling of 3D EM fields with scalar and vector potentials. In: *Three-dimensional electromagnetics*. Houston, TX: Society of Exploration Geophysicists, pp. 146–160.

Pardo, D. & Torres-Verdín, C. (2015) Fast 1D inversion of logging-while-drilling resistivity measurements for improved estimation of formation resistivity in high-angle and horizontal wells. *Geophysics*, 80(2), E111–E124.

Puzyrev, V., Torres-Verdín, C. & Calo, V. (2018) Interpretation of deep directional resistivity measurements acquired in high-angle and horizontal wells using 3-D inversion. *Geophysical Journal International*, 213(2), 1135–1145.

Rabinovich, M., Le, F., Lofts, J.J. & Martakov, S. (2012) The vagaries and myths of look-around deep-resistivity measurements while drilling. *Petrophysics*, 53(02), 86–101.

Seydoux, J., Legendre, E., Mirto, E., Dupuis, C., Denichou, J.M., Bennett, N., et al. (2014) Full 3D deep directional resistivity measurements optimize well placement and provide reservoir-scale imaging while drilling. SPWLA-2014-LLLL. In: *SPWLA 55th annual logging symposium*, Abu Dhabi, UAE, May 2014. OnePetro.

Shahriari, M., Rojas, S., Pardo, D., Rodríguez-Rozas, A., Bakr, S.A., Calo, V.M., et al. (2018) A numerical 1.5 D method for the rapid simulation of geophysical resistivity measurements. *Geosciences*, 8(6), 225.

Sinha, S., Walmsley, A., Clegg, N., Vicuña, B., McGill, A., dos Reis, T.P. et al. (2022) Past, present and future applications of ultra-deep directional resistivity measurements: a case history from the Norwegian continental shelf. : SPWLA-2022-0045. In: *SPWLA 63rd annual logging symposium*. OnePetro.

Spies, B.R. (1989) Depth of investigation in electromagnetic sounding methods. *Geophysics*, 54(7), 872–888.

Thiel, M. & Omeragic, D. (2020) Full 3D reservoir mapping using deep directional resistivity measurements. SPE-201281-MS. In: *SPE annual technical conference and exhibition*. OnePetro.

Yee, K. (1966) Numerical solution of initial boundary value problems involving Maxwell's equations in isotropic media. *IEEE Transactions on Antennas and Propagation*, 14(3), 302–307.

APPENDIX A: REFERENCE FORMULAS

Electromagnetic fields

The partial differential equations governing the coupled scalar-vector potentials are given by

$$\nabla^2 \mathbf{A} - i\omega\mu_0\boldsymbol{\sigma}\mathbf{A} - \mu_0\boldsymbol{\sigma} \cdot \nabla V = -\mu_0 i\omega\epsilon\mathbf{E}, \qquad (A.1)$$

and

$$i\omega\nabla \cdot (\boldsymbol{\sigma}\mathbf{A}) + \nabla \cdot (\boldsymbol{\sigma}.\nabla V) = \nabla \cdot i\omega\epsilon\mathbf{E}, \qquad (A.2)$$

where $\mathbf{A}$ is a vector potential that satisfies the Coulomb gauge, $\mathbf{V}$ is the total electric scalar potential and $\mu_0 = 4\pi \times 10^{-7}$ (H/m). Three components of the vector potential are sampled on Yee's staggered grid and are located at the centre of the edges of the cell, whereas the scalar potential V is sampled on a standard grid at the corner of the cell. The above formulation assumes that the EM fields are excited in a general anisotropic medium, whose electrical conductivity (inverse of resistivity) is an arbitrary tensor $\sigma = \sigma(x, y, z)$, and ϵ is dielectric permittivity (LaBrecque, 1999). ω is the angular frequency ($2\pi f$), where f is the linear operating frequency of the EM instrument. Conductivity σ is required on cell edges because that is where the electric field is discretized. It is calculated as averaged conductivities of all neighbouring cells and is defined as a symmetric 3-by-3 tensor (Hou et al., 2006).

The conductivity tensor

Following Anderson et al. (2001), the uni-axial conductivity tensor with principal axes having strike ϕ and dip θ with respect to bed boundaries is given by

$$\begin{bmatrix} \sigma_{XX} & \sigma_{XY} & \sigma_{XZ} \\ \sigma_{YX} & \sigma_{YY} & \sigma_{YZ} \\ \sigma_{ZX} & \sigma_{ZY} & \sigma_{ZZ} \end{bmatrix}, \qquad (A.3)$$

with

$$\sigma_{XX} = \sigma_h + (\sigma_v - \sigma_h)\sin^2\theta\cos^2\phi, \qquad (A.4)$$

$$\sigma_{XY} = (\sigma_v - \sigma_h)\sin^2\theta\sin\phi\cos\phi, \qquad (A.5)$$

$$\sigma_{XZ} = (\sigma_v - \sigma_h)\sin\theta\cos\theta\cos\phi, \qquad (A.6)$$

$$\sigma_{YY} = \sigma_h + (\sigma_v - \sigma_h)\sin^2\theta\sin^2\phi, \qquad (A.7)$$

$$\sigma_{YZ} = (\sigma_v - \sigma_h)\sin\theta\cos\theta\sin\phi, \qquad (A.8)$$

$$\sigma_{ZZ} = \sigma_v - (\sigma_v - \sigma_h)\sin^2\theta, \qquad (A.9)$$

where X, Y and Z are well trajectory coordinate systems, θ is the z-axis rotation from the formation coordinate to the well trajectory coordinate system, ϕ is the y-axis rotation from the formation coordinate to the well trajectory coordinate system and σ_h and σ_v are the conductivity in the horizontal and vertical directions, respectively.

Skin depth formula

Skin depth depends on the properties of the conductor, that is, its size, resistivity, magnetic permeability as well as the frequency of the signal. To calculate skin depth, we used the following formula:

$$\delta = \sqrt{\frac{\rho}{\omega\mu_0\mu_r}}, \qquad (A.10)$$

where δ is skin depth, ρ is the effective resistivity of conductive formations, ω is the angular frequency ($2\pi f$) of the electromagnetic instrument, μ_0 is the permeability of free space and μ_r is the relative magnetic permeability of the conductor.

APPENDIX B: VERIFICATION

To verify the accuracy and reliability of our three-dimensional (3D) finite-volume solver (Hou et al., 2006), we constructed a synthetic formation with three homogeneous layers (see Figure B.1) and compared the corresponding results to those obtained with a semi-analytical one-dimensional (1D) solver (Pardo & Torres-Verdín, 2015) and (Shahriari et al., 2018). Electromagnetic measurements were calculated assuming an inclined well trajectory across the 1D formation. The measurements are taken at the middle of the midpoint of the transmitter–receiver spacing, and after post-processing they are transferred to the position of the transmitter for plotting.

Figure B.2 compares the 3D finite-volume results to those obtained with the 1D semi-analytical algorithm. For all coupled (XX, YY and ZZ) and cross-coupled magnetic field components, both for real and imaginary parts, there is less than a 1% difference between 1D and 3D results. Cross-coupled components of magnetic fields with Y are zero; hence, they are not included in the comparison.